

## Mirage effect from thermally modulated transparent carbon nanotube sheets

This article has been downloaded from IOPscience. Please scroll down to see the full text article.

2011 Nanotechnology 22 435704

(<http://iopscience.iop.org/0957-4484/22/43/435704>)

View [the table of contents for this issue](#), or go to the [journal homepage](#) for more

Download details:

IP Address: 129.110.5.92

The article was downloaded on 04/10/2011 at 16:53

Please note that [terms and conditions apply](#).

# Mirage effect from thermally modulated transparent carbon nanotube sheets

Ali E Aliev<sup>1</sup>, Yuri N Gartstein<sup>2</sup> and Ray H Baughman<sup>1</sup>

<sup>1</sup> Alan G MacDiarmid NanoTech Institute, University of Texas at Dallas, Richardson, TX 75083, USA

<sup>2</sup> Department of Physics, University of Texas at Dallas, Richardson, TX 75083, USA

E-mail: [Ali.Aliev@utdallas.edu](mailto:Ali.Aliev@utdallas.edu)

Received 9 June 2011, in final form 29 August 2011

Published 3 October 2011

Online at [stacks.iop.org/Nano/22/435704](http://stacks.iop.org/Nano/22/435704)

## Abstract

The single-beam mirage effect, also known as photothermal deflection, is studied using a free-standing, highly aligned carbon nanotube aerogel sheet as the heat source. The extremely low thermal capacitance and high heat transfer ability of these transparent forest-drawn carbon nanotube sheets enables high frequency modulation of sheet temperature over an enormous temperature range, thereby providing a sharp, rapidly changing gradient of refractive index in the surrounding liquid or gas. The advantages of temperature modulation using carbon nanotube sheets are multiple: in inert gases the temperature can reach  $>2500$  K; the obtained frequency range for photothermal modulation is  $\sim 100$  kHz in gases and over 100 Hz in high refractive index liquids; and the heat source is transparent for optical and acoustical waves. Unlike for conventional heat sources for photothermal deflection, the intensity and phase of the thermally modulated beam component linearly depends upon the beam-to-sheet separation over a wide range of distances. This aspect enables convenient measurements of accurate values for thermal diffusivity and the temperature dependence of refractive index for both liquids and gases. The remarkable performance of nanotube sheets suggests possible applications as photo-deflectors and for switchable invisibility cloaks, and provides useful insights into their use as thermoacoustic projectors and sonar. Visibility cloaking is demonstrated in a liquid.

 Online supplementary data available from [stacks.iop.org/Nano/22/435704/mmedia](http://stacks.iop.org/Nano/22/435704/mmedia)

(Some figures in this article are in colour only in the electronic version)

## 1. Introduction

Photothermal deflection (PTD), otherwise known as the mirage effect, is a naturally occurring optical phenomenon caused by the refraction gradient created by a hot surface. A commonly observed example of the mirage effect is the 'puddle of water' that seems to appear when a heated road surface is viewed from a distance, which is due to the bending of light by the refractive index gradient in the air above the road surface, so that the observer sees the sky instead of the road. In 1979 Boccara *et al* demonstrated the use of PTD for monitoring temperature gradients close to and within a material [1], which led to more recent theoretical and experimental advances [2–5]. This method, which involves the detection of refractive index gradients associated with temperature gradients, has been

successfully used for thermal diffusivity measurements in gases, liquids and solids.

The present goal is to evaluate application of a highly aligned, free-standing multi-walled carbon nanotube (MWNT) sheet as a highly controllable, rapidly switchable heat source for effective beam deflection in gases and liquids. More generally, derived experimental and theoretical results on the frequency dependence of heat transfer from nanotube sheets to surrounding liquids and gases will be useful for the optimization of thermoacoustic devices, such as loudspeakers and sonar projectors. These thermoacoustic devices exploit the advantages of carbon nanotube sheets as a robust system for rapid heat transfer to liquids and gases: (1) giant gravimetric surface area (which can exceed  $300 \text{ m}^2 \text{ g}^{-1}$ ), (2) high thermal stability, (3) high thermal and electrical conductivities,

(4) areal densities that can be lower than  $3 \mu\text{g cm}^{-3}$  and (5) specific strengths that can exceed that of steel plate.

These aerogel sheets are directly produced by mechanical drawing from special nanotube forests that are grown by chemical vapor deposition. Highly efficient sound generation in air [6] and underwater [7] using free-standing, supported or encapsulated MWNT sheets have been recently demonstrated for a wide frequency range. Due to the extremely low heat capacity of MWNT aerogel sheets and the correspondingly low thermal inertia (resulting from low volumetric density,  $\sim 1.5 \text{ mg cm}^{-3}$ , and low areal density,  $\sim 3 \mu\text{g cm}^{-2}$ ), the sheet temperature synchronizes with electrical current in a wide frequency range,  $10^{-3}$ – $10^5$  Hz. We will show that high beam deflection efficiency results from the exceptionally high thermal interaction of a carbon nanotube network with surrounding media, as a consequence of the extremely high accessible internal surface area and high thermal conductivity of individual carbon nanotubes. We investigate the peculiarities of photothermal deflection in gases and liquids, and analyze optimal conditions for laser beam deflection using thin, self-supported carbon nanotube sheets that are either aligned or highly disordered and comprise either multi-walled or single-walled (SWNTs) carbon nanotubes.

Measurements are made [1] by using an electrical heating element, which heats up a surrounding medium, so as to generate a refractive index gradient (RIG) that is directed away from the surface. A laser probe beam propagating normal to the RIG and parallel to the hot surface suffers deflection from the original beam path (mirage effect) as it passes through the region above the heated surface. The extent of the deflection, which is a function of the RIG in the vicinity of the surface, depends on thermal parameters of the heater and the surrounding medium, as well as the heat transfer rate between the heater and surrounding medium.

Optical deflectors are important for optical scanning, optical communication and optical data processing, and various types of deflectors have been proposed to date [8]. Most optical deflectors utilize mechanical rotation of mirrors or holograms, which is suitable for such applications as laser projectors and laser printers. Laser scanning by acousto-optical deflectors (AODs) does not involve actual mechanical movement and thus provides rapid scanning, high precision and stability. AOD changes the direction of a laser beam by diffraction of the laser beam on a grating produced by acoustic waves. The angular deflection of the beam is linearly proportional to the acoustic frequency, so the higher the frequency, the larger the diffracted angle:  $\theta \approx \lambda_0 f_a / V_a$ , where  $\lambda_0$  is the optical wavelength in air,  $V_a$  is the acoustic velocity and  $f_a$  is the deployed acoustical frequency. While commercial AODs based on  $\text{TeO}_2$ , GaP,  $\text{LiNbO}_3$  and fused silica are widely available for acoustic frequencies above 10 MHz, the modulation of the deflection angle at low frequencies is challenging. Moreover, the existence of high intensity (zero-order) direct laser beams is undesirable for many applications.

Electro-optic modulators and deflectors, mostly based on Kerr and Pockels effects, exhibit higher speed and larger bandwidth than competing technologies (mechanical and acousto-optic devices), but have relatively small numbers

of resolvable spots, limited beam-diameter capabilities and require high operating voltage. Because of these factors and the relatively high price of electro-optic crystals electro-optic deflectors are used for few applications. Most of the work done on electro-optic deflectors has been experimental; relatively few commercial models are available [9]. In addition, electro-optic and acousto-optic devices are bulky, require high drive power and have low compatibility for integrated circuits.

We here demonstrate large angle deflection of a laser beam by using  $20 \mu\text{m}$  thick, optically transparent carbon nanotube sheets that are electrically heated at any of a wide range of frequencies (1 mHz–100 kHz in gases and 1 mHz–100 Hz in liquids). This approach provided a great flexibility and accuracy in controlling the deflection angle. The possibility of optical and acoustical cloaking devices, which could render objects invisible by deflecting light or ultrasound beams around them, is suggested by the obtained results.

## 2. Experimental details

Transparent, highly oriented MWNT sheets were drawn from the sidewall of a 300–350  $\mu\text{m}$  tall MWNT forest, which was synthesized by catalytic chemical vapor deposition (CVD) of acetylene gas [10]. Figure 1(a) is a scanning electron microscope (SEM) image of a suspended MWNT sheet that is supported by two parallel electrodes of a photothermal cell and figures 1(b) and (c) are photographs of the same MWNT sheet in unheated (b) and incandescent (c) states. The details of the experimental set-up and the gases and liquids used are presented in supplementary data available online (supporting material, available at [stacks.iop.org/Nano/22/435704/mmedia](http://stacks.iop.org/Nano/22/435704/mmedia)).

## 3. Simulation of beam deflection in various gases

The mirage deflection angle for the collinear configuration is given by [2]

$$\theta_c(x) = -\frac{1}{n} \frac{dn}{dT} \int_{-l/2}^{l/2} \nabla T_g \times dl, \quad (1)$$

where  $l$  is the interaction pathway of the probe beam (which is approximately the sheet dimension along the beam path) and  $\nabla T_g$  is the temperature gradient ( $dT/dx$ , for a collinear beam interacting with a planar heat wave), where  $x$  is the distance between the heated plane and the beam, and  $n$  is the refractive index of the medium. By ignoring small variations with wavelength, the index of refraction  $n$  for the gases is only weakly temperature-dependent:

$$n = 1 + \frac{n_0 - 1}{1 + \delta T}. \quad (2)$$

Because of the small value of the temperature coefficient  $\delta = (273.15 \text{ K})^{-1}$  and the small refractive index of inert gases at atmospheric pressure ( $n_0 - 1 < 0.0003$ ), the bending of light is usually extremely small ( $10^{-4}$  radian for  $\Delta T = 200 \text{ K}$  [2]).

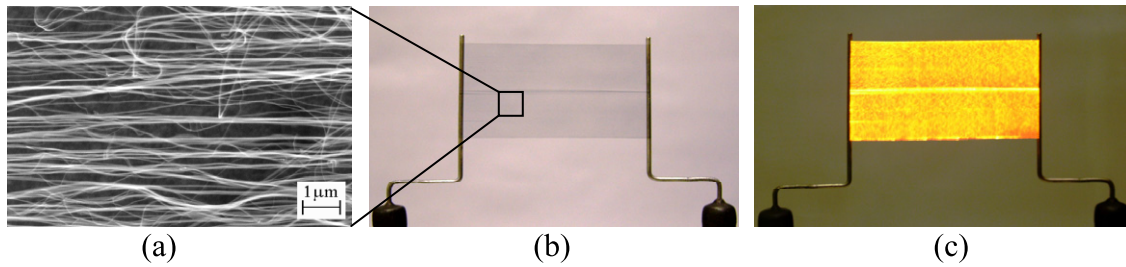


**Figure 1.** (a) SEM image of a self-supported, aligned MWNT sheet that was drawn from an MWNT forest. (b) Photograph of the  $2.5 \times 5 \text{ cm}^2$  MWNT sheet of (a), which is attached under tension between two copper electrodes. The box shows the approximate region of the sheet where the SEM image of (a) was obtained. (c) Photograph showing incandescence, by radiation of polarized light, for this MWNT sheet when it is resistively heated at  $\sim 1650 \text{ K}$ .

**Table 1.** The refractive index and some thermodynamic parameters of studied media: air, argon (Ar), helium (He), methanol (Mth), ethanol (Eth), chlorobenzene ( $\text{C}_6\text{H}_5\text{Cl}$ ), carbon tetrachloride ( $\text{CCl}_4$ ) and diiodomethane ( $\text{CH}_2\text{I}_2$ ) [11].  $T = 25 \text{ }^\circ\text{C}$ .

	Air	Ar	He	Mth	Eth	$\text{C}_6\text{H}_5\text{Cl}$	$\text{CCl}_4$	$\text{CH}_2\text{I}_2$
$(n - 1) \times 10^3$ at 633 nm	0.276	0.281	0.036	326.3	360.4	524.8	459	742.8
$-dn/dT \times 10^{-4} (\text{K}^{-1})$	0.0087	0.0089		4.0	3.97	5.73	6.12	
$\alpha_1 (\text{mm}^2 \text{ s}^{-1})$	23	17.8	163	0.099	0.085	0.0858	0.073	0.061
$\alpha_m (\text{mm}^2 \text{ s}^{-1})$	23.2	17.9	165	0.100	0.086	0.086	0.071	0.061
$l_{(5 \text{ Hz})} (\text{mm})$	1.2	1.064	3.22	0.080	0.074	0.074	0.068	0.062
$\rho_o (\text{kg m}^{-3})$	1.2	1.784	0.1786	792	789	1106	1587	3325
$C_p (\text{kJ m}^{-3} \text{ K}^{-1})$	1.2042	0.9282	0.9275	2020	1920	1480	1350	1661
$\kappa (\text{W m}^{-1} \text{ K}^{-1})$	0.025	0.0177	0.1513	0.202	0.169	0.127	0.099	0.1015

Ignoring the contribution from acoustical waves [2, 5], the periodically varying thermal wave component perpendicular to the sheet plane at a distance  $x$  from this plane is

$$T = T_o \exp(-kx) \cos(\omega t - kx), \quad (3)$$

where the temperature of the planar heat source is varied periodically as  $T_o \cos \omega t$  and  $k = (\omega/2\alpha)^{1/2}$  is the wavenumber of the temperature wave, which is the reciprocal of the thermal diffusion length,  $l_D = (\alpha/\pi f)^{1/2}$ . Here  $\omega = 2\pi f$  and  $\alpha$  is the thermal diffusivity.

Numerical simulation of equation (3) for three gases (air, argon and helium) at 5 Hz temperature modulation frequency and in argon at three frequencies (see figure S2 in the supplementary information available at [stacks.iop.org/Nano/22/435704/mmedia](http://stacks.iop.org/Nano/22/435704/mmedia)) clearly shows the frequency limits of photothermal beam deflection in gases with low thermal diffusivity (e.g. air and argon). Since practically all of the expansion effect due to the periodic change in temperature takes place within the region bounded by the thermal wavelength  $\lambda = 2\pi l_D$  the usable beam diameter at high frequencies cannot exceed  $\lambda/2$ . Beyond this limit the thermal gradient (and  $dn/dT$ ) changes sign. For example, in argon at a thermal modulation frequency of 100 kHz the beam diameter should be below  $\pi l_D = 13.5 \mu\text{m}$ , which is close to the optical limit for a non-divergent laser beam. At the same time, to get an appreciable change in refractive index across the beam in helium at low frequency (5 Hz) the beam diameter should be above 5 mm.

While the same limitations on photothermal deflection are valid for liquids, the thousand times higher densities of liquids make them a more useful media for providing large deflection

angles. On the other hand, the higher liquid density increases the heat capacity of system and correspondingly reduces the obtainable rate for modulation of the beam deflection angle. Table 1 provides the parameters needed for the above simulations, as well as other useful parameters that will be used in further discussion.

In the above table  $n$  is the refractive index,  $\alpha_1$  and  $\alpha_m$  are the thermal diffusivity from the literature and measured in this work, respectively,  $l_{(5 \text{ Hz})}$  is the thermal diffusion length calculated for a thermal modulation frequency of  $f = 5 \text{ Hz}$ ,  $\rho_o$  is the density,  $C_p$  is the volumetric heat capacity and  $\kappa$  is the thermal conductivity. Note that the slope of the linear relation between the phase ( $\varphi_c$ ) of a periodically deflecting beam as a function of the separation between a planar heat source and laser beam ( $x$ ) is often used for thermal diffusivity measurements of a medium that contacts the heat source [3, 5]:

$$\frac{\Delta\varphi}{\Delta x} = \sqrt{\frac{\omega}{2\alpha}}. \quad (4)$$

## 4. Results and discussion

### 4.1. Black-body radiation from MWNT sheets

To estimate the intrinsic thermal inertia of a single MWNT sheet, we studied the intensity of black-body radiation from this sheet in vacuum and in argon gas as a function of the ac frequency deployed for resistive sheet heating. Unlike for a short ( $1.3 \mu\text{m}$ ) arc-discharge grown single MWNT [12], the thermal inertia of a large-area CVD-grown large MWNT sheet suspended in vacuum is overwhelmingly dominated above 150 K by radiation [13]. Taking into account the high aspect

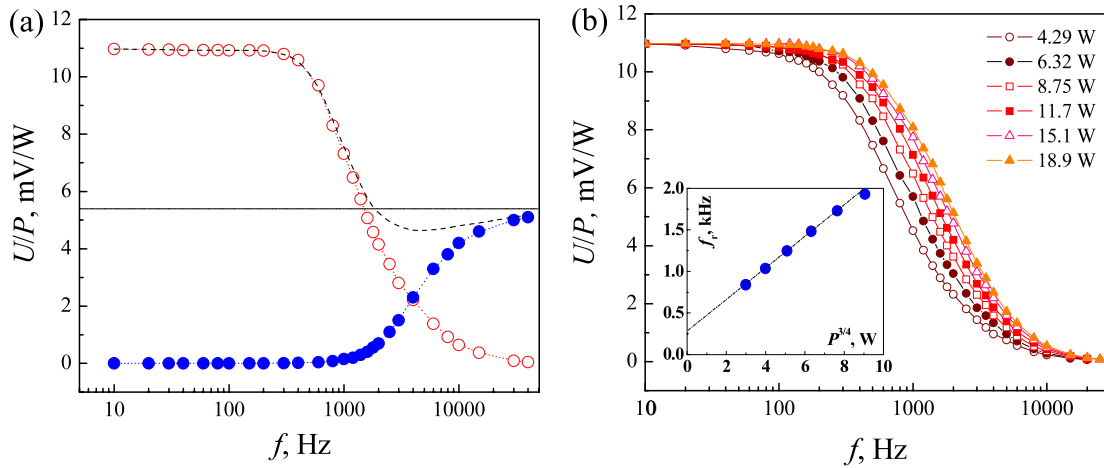


**Figure 2.** The frequency dependence of black-body radiation intensity (measured in mV, and normalized to applied electrical power) from a single MWNT sheet ( $2.5 \times 5 \text{ cm}^2$ ) in vacuum. (a) Open (red) and solid (blue) circles show the normalized intensities of the modulated and non-modulated parts of incandescent radiation for 15 W applied power, corresponding to a measured black-body temperature of about  $1500 \pm 50 \text{ K}$ . The dashed curve is a calculated sum of both parts. (b) The frequency dependence of the modulated part of normalized radiation intensity taken at six levels of applied power. The left bottom inset shows the linear increase of onset frequency  $f_r$  versus applied power,  $P^{3/4}$ .

ratio of CVD-grown MWNTs ( $L/D \sim 4 \times 10^4$ ), the heat dissipation by lateral black-body radiation ( $P_{\text{rad}} \sim 15 \text{ W}$  at  $T = 1500 \text{ K}$ ) in vacuum is three orders higher than through direct thermal conduction of carbon nanotubes to the thermal sink ( $P_{\kappa} = 10^{-2} \text{ W}$ ,  $\kappa_{\text{MWNT}} = 600 \text{ W m}^{-1} \text{ K}^{-1}$  [14]). As shown below, we surprisingly find that in vacuum the onset of the frequency dependence of radiation intensity increases considerably with the applied power,  $f_r \sim P^{3/4}$ .

Figure 2(a) shows the dependence of black-body radiation intensity on thermal modulation frequency for a large MWNT sheet ( $2.5 \times 5 \text{ cm}^2$ ) in  $\sim 0.1 \text{ mTorr}$  vacuum. Since the output voltage of the present photodetector linearly depends upon the incident light intensity (see figure S2(a) in the supplementary information available at [stacks.iop.org/Nano/22/435704/mmedia](http://stacks.iop.org/Nano/22/435704/mmedia)), for simplicity we used voltage (mV units) to describe light intensity in figure 2(a). The transparency of the sheet at 550 nm wavelength was  $\sim 85\%$  and the electrical resistance was  $\sim 2.1 \text{ k}\Omega$ . The modulated component of incandescent radiation starts decreasing at  $\sim 300 \text{ Hz}$  and vanishes into the noise at about 100 kHz. The decrease of the modulated component is accompanied by a gradual increase of the non-modulated background incandescence. This is expected if heat loss is predominantly through radiation, since the sum of modulated ( $P_{\sim}$ ) and non-modulated ( $P_{-}$ ) irradiated power should equal the applied electrical power  $P$ :  $P \approx P_{\sim} + P_{-}$ . The small asymmetry of these two components results from the low sensitivity of the liquid-nitrogen-cooled infrared photodetectors used in the far-infrared (see ‘experimental’ in the supplementary information available at [stacks.iop.org/Nano/22/435704/mmedia](http://stacks.iop.org/Nano/22/435704/mmedia)). For comparison, the decrease of modulated light intensity, and the increase of non-modulated intensity, for a 12  $\mu\text{m}$  tungsten filament (50 cm long) starts at  $\sim 1 \text{ Hz}$ , and at 100 Hz the modulated part does not exceed 5% of the total radiation intensity.

The onset frequency  $f_r$  is defined as the thermal frequency at which the root-mean-square intensity of the modulated parts

of incandescent emission decreases to one-half of its value at low frequencies. In agreement with the experimental results of figure 2(b), theoretical analysis of the heat balance equation (see the supplementary information available at [stacks.iop.org/Nano/22/435704/mmedia](http://stacks.iop.org/Nano/22/435704/mmedia)) shows that the onset frequency,  $f_r$  for a modulated radiation component linearly depends upon the applied power,  $P^{3/4}$ :

$$\frac{f_r}{f'} = \frac{(2A\varepsilon\sigma)^{1/4}}{4V\rho C_p} P^{3/4}, \quad (5)$$

where  $P = I^2 R$  is the amplitude of the input power delivered by the electric current  $I$  at frequency  $f$  that produces a thermal fluctuation at  $f_r = 2f$ , while  $f'$  is a dimensionless scaling factor for  $f_r$ ,  $\varepsilon$  is the emissivity,  $\sigma = 5.67 \times 10^{-8} \text{ W m}^{-2} \text{ K}^{-4}$  is the Stefan–Boltzmann constant,  $\rho$  is the density,  $C_p$  is the heat capacity of the black-body radiation source, and  $A$  and  $V$  are the surface area and volume, respectively. The experimental data of the inset to figure 2(b) shows that  $f_r$  linearly increases with  $P^{3/4}$ . Normalizing the scaled frequency using the factor  $P^{3/4}$  provides a universal curve that agrees with data at all power levels.

We observed a remarkable shift of radiation intensity onset towards higher frequencies ( $\Delta f_r = 500 \text{ Hz}$ ) for an MWNT sheet drawn from a  $\sim 180 \mu\text{m}$  tall forest (95% transparency at 632 nm), compared with that for the 350–400  $\mu\text{m}$  tall forests (85% transparency at 632 nm) used for the study of figure 2. This shift is consistent with the observation that a decrease in forest height generally decreases nanotube bundling and increases sheet transparency, since these changes decrease thermal inertia and increase radiative heat loss per areal mass.

Figure 3(a) compares the frequency dependence of modulated black-body radiation in vacuum for three different arrangements of MWNT and SWNT films. The onset frequency ( $\sim 2.1 \text{ kHz}$ ) observed for short electrode distances (2.5 mm) in figure 3(a) is consistent with the ramp-up (0.8 ms) and ramp-down (0.7 ms) times previously observed for pulse

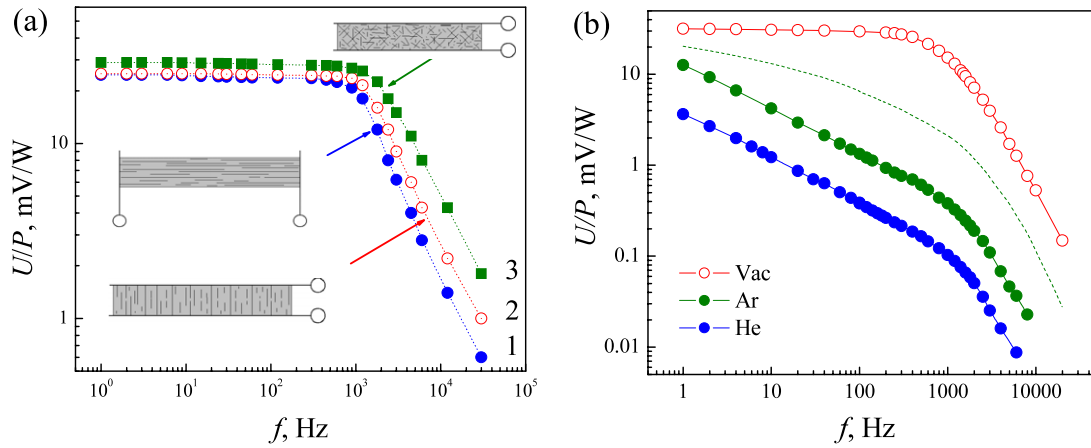


**Figure 3.** (a) The frequency dependence of black-body radiation for a  $25 \times 2 \text{ mm}^2$  suspended MWNT sheet with nanotubes aligned parallel to the long side (1), a  $2 \times 25 \text{ mm}^2$  MWNT sheet with nanotubes aligned perpendicular to the long side (2) and a  $2 \times 25 \text{ mm}^2$  randomly deposited suspended SWNT sheet (3). The ac current was applied along the nanotube alignment direction for MWNT sheets and along the short side in an SWNT sheet. (b) The frequency dependence of black-body radiation for a  $25 \times 50 \text{ mm}^2$  MWNT sheet in vacuum (open red circles), in argon (solid green circles) and in helium (solid blue circles) at ambient pressure. For all experiments except for the dashed curve for argon (where  $P = 17.3 \text{ W}$  and  $T_{10 \text{ Hz}} = 1000 \pm 50 \text{ K}$ ), the applied power was  $10 \text{ W}$ .

heating of similar  $2.5 \text{ mm}$  long and  $8 \text{ mm}$  wide aligned MWNT sheets [15]. Thin, self-supporting SWNT sheets containing randomly oriented nanotubes (prepared by filtration) exhibit a slightly higher frequency onset  $f_r$  ( $\sim 3 \text{ kHz}$ , corresponding to lower thermal inertia) than for forest-drawn sheets ( $\sim 1.5 \text{ kHz}$ ) having similar transparency. Severe bundling for SWNTs, which creates a main conductive path for resistive heating, still keeps the onset frequency below  $3 \text{ kHz}$  (compared to  $1.6 \text{ MHz}$ , which is calculated from  $0.1 \mu\text{s}$ , the time during which the  $1.3 \mu\text{m}$  suspended single MWNT reaches steady-state incandescence [12]).

The highly porous structure of an aerogel-like MWNT sheet enhances thermal interactions with surrounding gases, thereby decreasing the temperature and corresponding black-body radiation output that results from a given electrical power input. Figure 3(b) shows the frequency dependence of black-body radiation intensity per input power from a large-area MWNT sheet ( $25 \times 60 \text{ mm}^2$ ) in argon and helium at ambient pressure (760 Torr). For comparison, the corresponding data for an MWNT sheet in vacuum is also shown. The gradual linear decrease of modulated radiation with increasing frequency was observed for both gases in a wide frequency range, from  $1 \text{ Hz}$  to  $1 \text{ kHz}$ . The intrinsic thermal inertia of the sheet gives an additional contribution to the decline of modulated radiation intensity at higher frequencies. As a result of the second dissipation channel provided by gas heating, the frequency onset is shifted upwards in frequency by  $3\text{--}4 \text{ kHz}$ . The low frequency slopes of the modulated black-body radiation curves are proportional to the thermal diffusion lengths  $l_D = (\alpha/\pi f)^{1/2}$  of the gases. At high applied power ( $P > 15 \text{ W}$ ,  $T > 1000 \text{ K}$ ) the radiated and conductively dissipated parts of the energy transfer become comparable in argon gas. In the highest frequency regime, figure 3(b) shows that the modulated components of black-body radiation for in-gas and in-vacuum have about the same linear dependence on frequency. As the applied power is increased, so that radiative

heat loss is increased relative to conductive heat loss, the in-gas curves of modulated radiation approach the in-vacuum results (dashed line in figure 3(b)). In argon and air (having about the same thermal inertia, see table 1 for  $\rho C_p$ ) the diffusion lengths become shorter than the thickness of the MWNT sheet ( $l_{10 \text{ kHz}} = 27 \mu\text{m}$ ) at frequencies above  $10 \text{ kHz}$ . Heat release from the depth of a  $20 \mu\text{m}$  aerogel film by direct exchange with the surrounding medium is then hampered. While the one-order-higher thermal conductivity of helium than for argon and air substantially suppresses overall radiation intensity, the curves in figure 3(b) for both gasses are similar.

#### 4.2. Photothermal deflection in gases

Photothermal experiments in gases and liquids demonstrate the advantages of thin, low thermal inertia MWNT sheets as electrically driven heaters for achieving the mirage effect. As a result of ac heating, an aerogel sheet produces planar thermal waves from opposite sheet sides, which produce the refractive index gradient needed for beam deflection. The mirage effect was characterized by measuring the angular deflection of a laser beam that was directed parallel to the sheet surface (see schematic diagram of the measurement in supplementary figure S1 available at [stacks.iop.org/Nano/22/435704/mmedia](http://stacks.iop.org/Nano/22/435704/mmedia)). A laser beam (He–Ne laser at  $632.8 \text{ nm}$ , with polarization parallel to the sheet surface) was directed in the length direction for a  $55 \text{ mm}$  long and  $6 \text{ mm}$  wide strip of a forest-drawn MWNT sheet, which was resistively modulated in air at various frequencies. Since the CNTs are readily oxidized in oxygen at elevated temperatures (in air  $T_{\text{max}} \sim 900 \text{ K}$ ) the temperature of the sheet in air was restricted to below  $600 \text{ K}$ . Figures 4(a) and (b) show the beam deflection angle dependence on separation distance from the sheet  $x$  and upon applied power  $P = I^2 R$ , respectively. The deflection angle decreases with increasing separation between the sheet and laser beam, in accordance with equation (1) and the simulation curves shown in figure S2 (available at [stacks.iop.org](http://stacks.iop.org)).

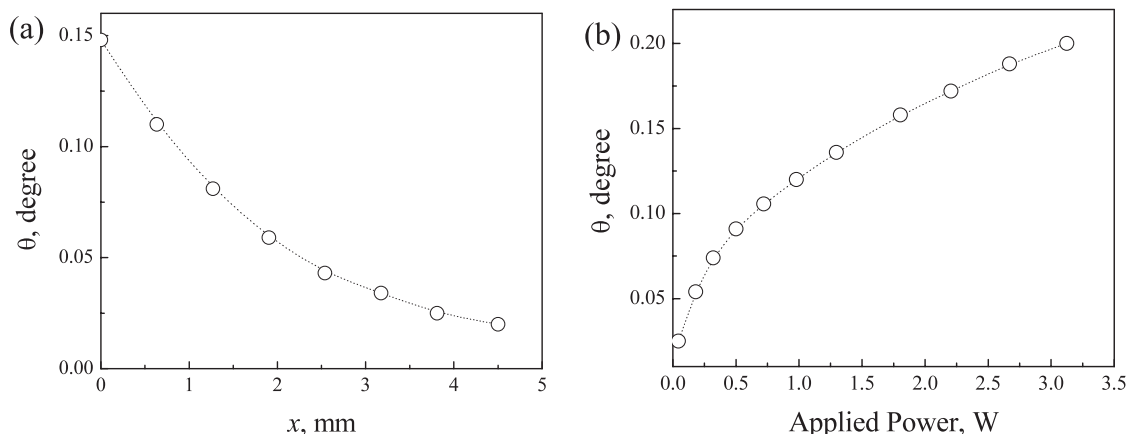


**Figure 4.** Photothermal deflection in air: (a) the deflection angle  $\theta$  as a function of the separation between the nanotube sheet plane and the laser beam ( $x$ ) for  $P = 1.14$  W and  $f = 10$  Hz. (b) The dependence of deflection angle upon the applied power.

[org/Nano/22/435704/mmedia](http://stacks.iop.org/Nano/22/435704/mmedia)). The saturation of deflection angle at high applied power (figure 4(b)) is likely due to an increased radiative contribution to heat dissipation, which does not contribute to heat exchange with the air.

For the purpose of using nanotube-based photothermal deflection for measuring the thermal diffusivity of contacting liquids or gases, we measured the modulation amplitude and phase of the deflected beam (with respect to the applied ac signal used for heating) as a function of the separation  $x$  between the laser beam and the MWNT sheet. The undeflected laser beam was half obscured from the window of an Si photodetector by using one side of a precision optical slit. Angular photothermal modulation moved the laser beam either into the slit or away from it, thereby producing a sinusoidal voltage signal at the detector. Figure 5(a) shows the beam modulated voltage from the photodetector as a function of beam separation distance from the sheet. The gases used were air, argon and helium—all measured at the same applied power of  $P = 10$  mW and an applied electrical frequency of 10 Hz (which produced the beam modulation at 20 Hz). For a wide range of separations between the sheet and the laser beam, the modulated part of the position-sensitive detector's (PSD) signal ( $U_m$ ) exponentially decreased with increasing distance  $x$ . The dependence, shown in figure 5(a), was used to determine the thermal diffusivity  $\alpha$  of the surrounding media by means of the equation,  $U_m = U_0 \exp\{-(\pi f/\alpha)^{1/2}x\}$ . We used power levels of below 0.1 W to avoid reflections of the thermal waves from the boundaries of the chamber walls. The solid lines in figure 5(a) show the calculated magnitude of the beam fluctuation:

$$U_m = 2\delta(n_0 - 1)\beta T_0 \exp(-x/l_D) \cos(\omega t), \quad (6)$$

using the thermal diffusivity and refractive index data from table 1. The heat exchange efficiency between heater and surrounding medium  $\beta$ , used as a fitting parameter, is two orders higher for a suspended MWNT sheet than for the often used thin platinum film [3]. Due to the low thermal diffusivity of argon ( $\alpha = 17.8 \text{ mm}^2 \text{ s}^{-1}$ ) at high frequencies, the temperature fluctuation region is reduced to the very

near vicinity of the MWNT sheet (see the right column for simulation in figure S3 available at [stacks.iop.org/Nano/22/435704/mmedia](http://stacks.iop.org/Nano/22/435704/mmedia)). Hence, use of a narrow laser beam provides the most reliable results.

The deflection angle  $\theta$  in helium is much smaller than in air or argon, which is consistent with the low refractive index and high thermal diffusivity of helium (see table 1 and simulations in the supplementary information available at [stacks.iop.org/Nano/22/435704/mmedia](http://stacks.iop.org/Nano/22/435704/mmedia)). The magnitude ( $U_m$ ) and phase ( $\varphi$ ) of the modulated signal in helium have much weaker dependences on separation distance  $x$ . To obtain a high deflection angle  $\theta$  at low frequencies, the beam cross section should be larger than 3–4 mm for helium. However, at high frequencies, the needed beam size for argon and air are reduced below practical limits. This problem can be avoided by the use of helium gas for photothermal deflection. Figure 5(c) shows that the frequency dependence of the magnitude of the modulated beam is dominated by the thermal inertia of surrounding gases, rather than the inertia of MWNT bundles.

#### 4.3. Photothermal deflection in liquids

The high hydrophobicity of carbon nanotubes to the water, which creates the tiny air-filled envelopes around each nanotube or bundle, is beneficial for underwater sound generation [7]. However, the additional interface causes high thermal resistance for temperature waves, which significantly complicates photothermal deflection (supplementary information). Moreover, water has an unusually high thermal conductivity ( $\kappa = 0.6 \text{ W mK}^{-1}$ ) and very low temperature coefficient of refractive index ( $dn/dT = -0.95$ ) which makes water unattractive for achieving high photothermal deflection [11].

For studying the mirage effect in liquids, we chose liquids that wet carbon nanotubes: methanol ( $\text{CH}_3\text{OH}$ ), ethanol ( $\text{C}_2\text{H}_5\text{OH}$ ), carbon tetrachloride ( $\text{CCl}_4$ ), chlorobenzene ( $\text{C}_6\text{H}_5\text{Cl}$ ) and diiodomethane ( $\text{CH}_2\text{I}_2$ ), which are here listed in order of increasing refractive index. Since the thermal inertia of a carbon nanotube film immersed in liquids is now mostly determined by the heat capacity ( $C_p$ ) and density ( $\rho$ ) of the

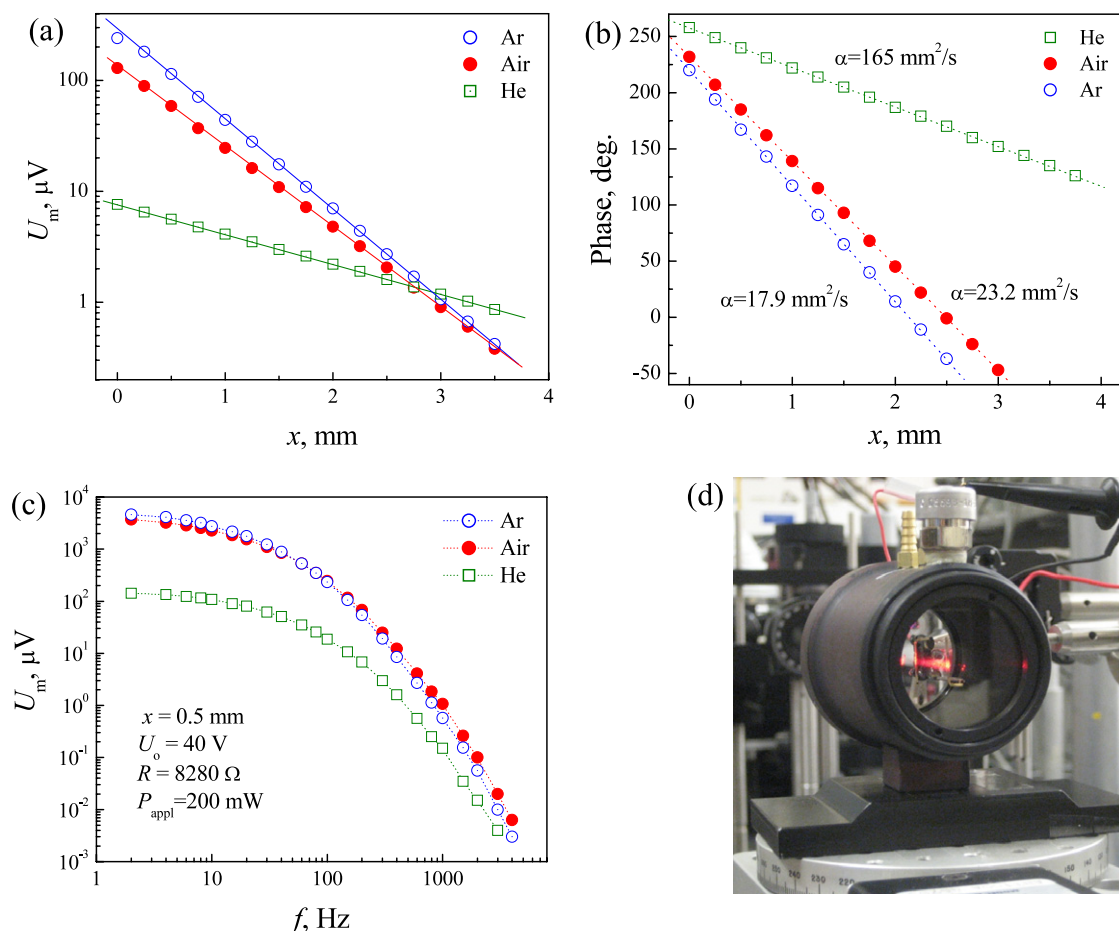


**Figure 5.** (a), (b) The decrease of PSD signal magnitude ( $U_m$ ) and phase ( $\varphi$ ) with increasing distance between the MWNT sheet and the laser beam ( $P = 10 \text{ mW}$ ,  $f = 20 \text{ Hz}$ ) in argon (open blue circles), in air (solid red circles) and in helium (open green squares). (c) The frequency dependence of the PSD signal in three selected gases. (d) The 32 mm inner diameter gas chamber, with temperature-controllable jacket, used to study selected gases.

liquids, the advantage of CNTs films for beam deflection is an extremely high interaction surface that enables efficient heat exchange. Figures 6(a) and (b) show, respectively, highly linear dependences of modulated signal ( $U_m$ ) and phase shift on the separation  $x$  between the sheet and the laser beam. Very low power was applied to the MWNT sheet,  $\sim 50 \text{ mW}$ , and the frequency was  $1 \text{ Hz}$ . The slope of these lines gives the thermal diffusivity of studied liquids with an accuracy of 1%. The signal due to thermal modulation decreases exponentially with increasing  $f$ , as shown in figure 6(c).

Since the intensity of modulated signal exponentially depends upon thermal diffusivity (equation (6)), the highest magnitude  $U_m$  was observed in methanol. However, the competition of high refractive index and low thermal diffusivity in heavy liquids like diiodomethane ( $\text{CH}_2\text{I}_2$ ) makes them very efficient at low frequencies,  $U_m(0.7 \text{ Hz}) = 12.5 \text{ mV}$ . Table 1 compares the presently measured thermal diffusivities for several liquids with literature data. The slightly higher presently obtained thermal diffusivities are due to local temperature rise (2–3 K) in the temperature-controllable, but unstirred, cell.

For relatively low applied power, an increase of applied power linearly increases the deflected beam position  $h$

(figure 7(a)), deflected angle  $\theta$  (figure 7(b)) and the modulation magnitude  $U_m$  (inset to figure 7(a)). At high applied power ( $P > 0.2 \text{ W}$ ) for all investigated liquids and gases we observed deviation from this linear behavior for both  $U_m(x)$  and  $\varphi(x)$ . An additional non-modulated component in beam deflection arises and increases with applied power and frequency. This component arises from thermal inertia of the liquid, which gives rise to the accumulation of heat in the vicinity of the MWNT heater, which dominates at  $f > 10 \text{ Hz}$  and  $P > 0.5 \text{ W}$ , as shown for  $\text{C}_6\text{H}_5\text{Cl}$  in the inset to figure 7(b).

#### 4.4. An invisibility cloak

Since beam deflection is proportional to the length of the heater along the path of the probe laser beam, it is easy to show that a 1 m long sheet will deflect the beam by over  $3^\circ$  in air (see figure 4(a)). A nanotube sheet covering suitable objects would produce a mirage, which could conceal objects on the Earth's surface that are viewed from a distance at a grazing angle (figure 8(a)). If the goal is to be able to switch the cloaking system on and off, then the nanotube sheet should have high transparency. To obtain at least 80% transparency for a tilted nanotube sheet having 85% transparency for orthogonally

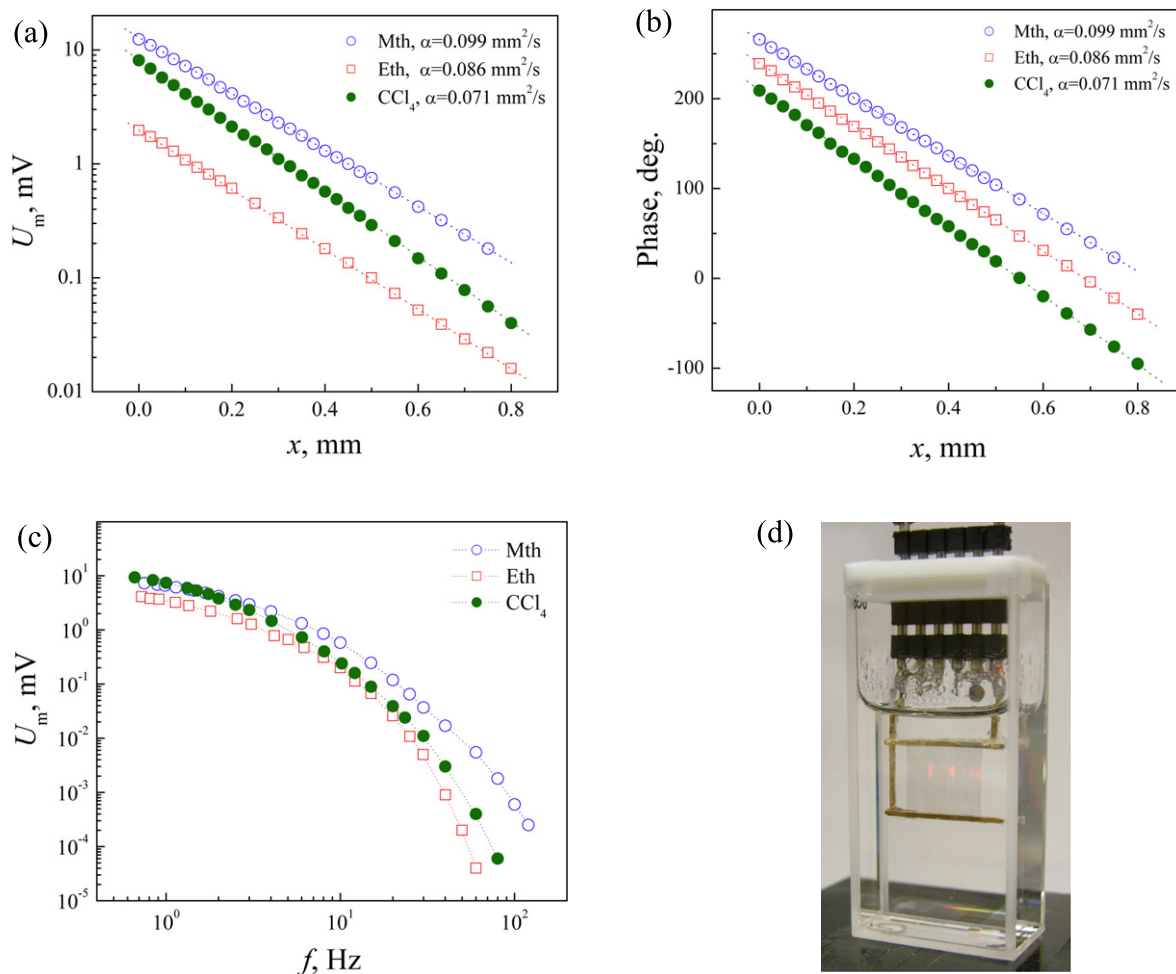


**Figure 6.** The magnitude (a) and phase (b) of modulated beam versus beam offset  $x$  in methanol (open blue circles), ethanol (open red squares) and carbon tetrachloride (solid green circles), measured for  $P = 50$  mW and  $f = 1$  Hz. (c) The frequency dependence of modulated beam detected by PSD in selected liquids. (d) Glass cell used for photothermal measurements in liquids, showing a free-standing MWNT sheet immersed in liquid. The nanotube alignment direction (vertical) is perpendicular to the laser beam (horizontal).

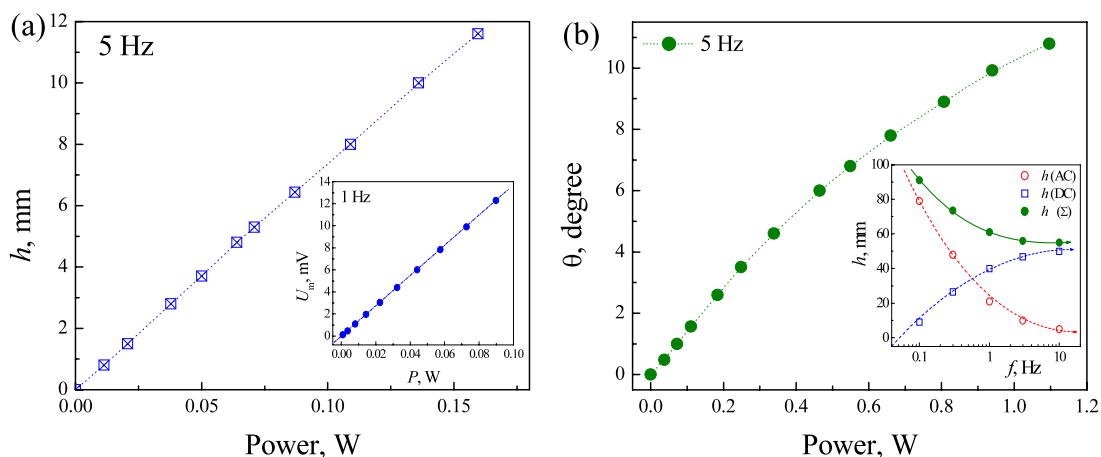


**Figure 7.** (a) The lateral deflection of the laser beam at 50 cm from the center of the glass cell versus applied power for a  $8.5 \times 20$  mm<sup>2</sup> MWNT sheet in methanol. The inset shows the magnitude of modulated beam (PSD signal) versus applied power. (b) The deflection angle versus applied power in C<sub>6</sub>H<sub>5</sub>Cl. The inset shows the frequency dependence of the modulated part of deflected beam ( $h$  (AC)), the non-modulated part ( $h$  (DC)) and the sum of both ( $h$  ( $\Sigma$ )).

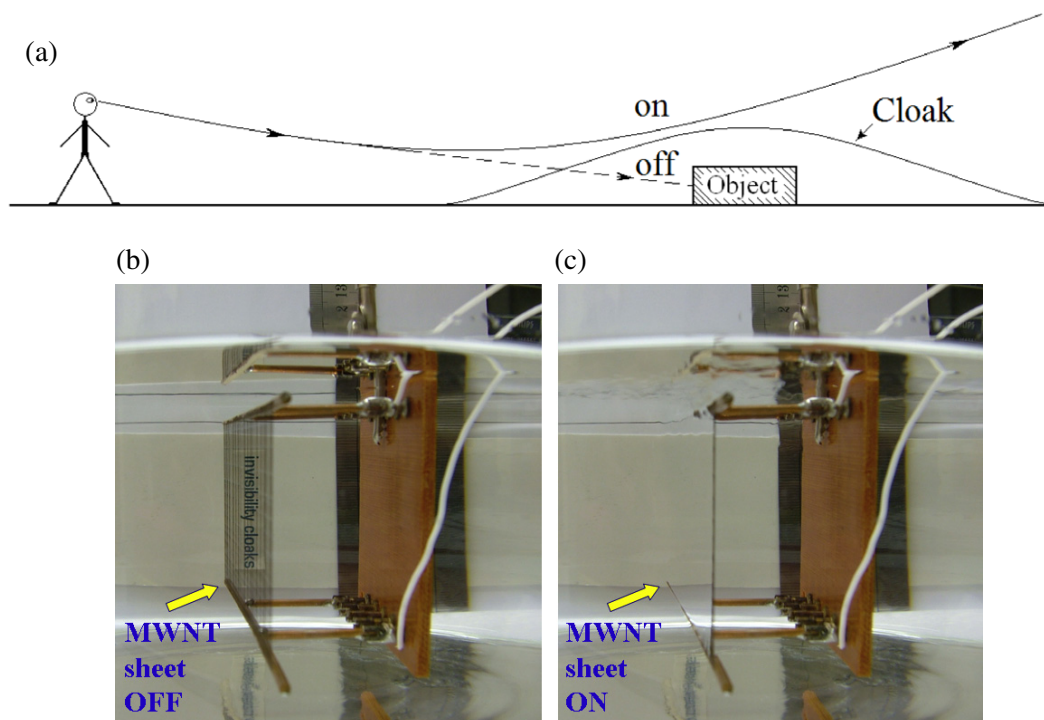


**Figure 8.** (a) Schematic diagram of large-area cloaking system. (b), (c) Underwater mirage effect created by  $5 \times 12 \text{ cm}^2$  MWNT sheet, ( $P = 6.6 \text{ W}$ ).

directed radiation, the grazing angle should be above  $6^\circ$ . To obtain a deflection angle of above  $6^\circ$ , the length of the sheet in the light propagation direction should be longer than 2 m. The CNT cloak can be activated (heated) resistively or by using electromagnetic pulses. The created gradient of refractive index will deflect light in the UV to infrared range.

For underwater application the grazing angle can be substantially higher due to the several-orders-higher gradient of refractive index, while the temperature gradient cannot exceed  $\sim 80^\circ\text{C}$ . An example of a switchable cloaking MWNT sheet in water is shown in the pictures of figures 8(b) and (c). The text ‘Invisibility cloaks’ attached to the sidewall of the glass container disappears when the MWNT sheet (tilted to  $\sim 5^\circ$  in front of the text) is switched resistively. The non-wetted surface of carbon nanotubes (provided by giant hydrophobicity, [7]) allows fast thermal switching of the very thin surrounding water layer. The total deflection response time in water is about 2 s ( $t_{\text{On}} < 0.5 \text{ s}$ ,  $t_{\text{Off}} > 1.5 \text{ s}$ ).

The cloaking systems in the visible is less attractive for underwater applications, namely for exploring a deep ocean, where darkness prevails. Nevertheless, a thin MWNT sheet, which is transparent to acoustical waves ( $T = 99\%$ ), can work as a perfect tunable reflector for high acoustical frequencies when switched thermally. The reason is as follows: the increased acoustical impedance of a thin heated water layer ( $Z = \rho V_s$ ) can substantially reduce the transmittance of the sheet and reflect (or deflect for given tilted angles) the acoustical beam. However, the reflectance and transmittance coefficients are frequency-dependent (see underwater acoustical cloaking in the supplementary information available at [stacks.iop.org/Nano/](http://stacks.iop.org/Nano/22/435704/mmedia)

[22/435704/mmedia](http://stacks.iop.org/Nano/22/435704/mmedia)) and little effect arises at low frequencies, when  $\lambda_s \gg l_D$  (i.e. below 300 kHz).

## 5. Conclusions

We demonstrated the advantages of free-standing carbon nanotube aerogel sheets for photothermal deflection in gases and liquids. The high observed performance of the carbon nanotube aerogel results from the giant porosity; low area density (a few  $\mu\text{g cm}^{-2}$ ), high thermal conductivity, high electrical conductivity and a gravimetric strength higher than that of a steel plate. The observed frequency range for photothermal modulation of the aerogel sheets is  $\sim 100 \text{ kHz}$  in gases and over 100 Hz in high refractive index liquids, and operation to over 2500 K is possible in inert gas. The heat exchange efficiency of these sheets is two orders higher than for the platinum foil that is commonly used as a heat source for photothermal deflection. Additionally, the carbon nanotube sheets have high optical and acoustic transparency. Both theoretically and experimentally we find in vacuum that the onset frequency for modulated incandescent radiation is increased with applied electrical power  $P$  as  $P^{3/4}$ . Normalizing the scaled frequency using the factor  $P^{3/4}$  provides a universal curve that agrees with data at all power levels.

The temperature-dependent onset for modulated black-body radiation at  $\sim 1000\text{--}2000 \text{ Hz}$  is consistent with the observed thermal inertia of large bundles which provide the main current pathways. Decreasing bundle size from the 100–150 nm diameter bundles existing in both aligned MWNT and randomly deposited SWNT sheets, while maintaining the

high porosity and low areal density of the aerogel sheets, will increase rate performance in liquids, gases and vacuum. Evidence for this is in the increased onset frequency for MWNT sheets grown from a decreased height forest, which display less bundling.

While such improvements are possible, the high temperature modulation rates of the present carbon nanotube aerogel sheets already enable fast, reliable measurements of thermal diffusivity and the temperature dependence of the refractive index for liquids and gases. These refractive measurements are facilitated by the long separation range where the intensity of the modulated laser beam and the phase of this beam (relative to the ac electrical input) linearly depend upon beam-to-sheet separation.

The high modulation rate achieved for incandescent radiation in vacuum (and the higher modulation rate in inert gas) suggests the use of the carbon nanotube aerogel sheets as the source of polarized light for active night vision systems that use phase-sensitive detection. The usually used filament arrays for these systems provide slow frequency response and light that is largely unpolarized. The high deflection angles and modulation rate in inert gases and non-wetting liquids enable use of these sheets for optical deflectors. The MWNT sheet-based light beam deflection devices possess a high degree of versatility, have a reasonably simple structure and are easily fabricated. Benefits over acousto-optic deflectors are the absence of an undeflected beam and elimination of the need for above 10 MHz acoustic waves to obtain high angle beam deflection. Their principal attraction, however, is for large, lightweight systems requiring wide-band aperiodic, rapid-access modes of operation. Low cost is a benefit over crystal-based deflectors based on Kerr and Pockels effects. Further development work is required before systems of this type can achieve their full potential. Specifically, effort should be directed towards high pressure xenon [ $(n - 1) \times 10^3 = 0.7$ ] encapsulated cells.

The optical and acoustical transparency of free-standing carbon nanotube films makes possible their use for large-area cloaking systems. Application of a nanotube sheet as a mirage-based concealment cloak is demonstrated in water. These nanotube sheets are of considerable interest for loudspeakers

and sonar projectors, and it is believed that this investigation of photothermal deflection will help optimize performance for these applications.

## Acknowledgments

We thank Marcio D Lima for providing drawable MWNT forests. This research work was supported by the Office of Naval Research MURI grant N00014-08-1-0654, NASA Phase II SBIR grant NAS-54C, the Air Force Office of Scientific Research grant FA9550-09-1-0537 and the Robert A Welch Foundation grant AT-0029.

## References

- [1] Boccara A C, Fournier D and Badoz J 1980 *Appl. Phys. Lett.* **36** 130–2
- [2] Murphy J C and Aamodt L C 1980 *J. Appl. Phys.* **51** 4580–6
- [3] Aamodt L C and Murphy J C 1981 *J. Appl. Phys.* **52** 4903–5914
- [4] Jackson W B, Amer N M, Boccara A C and Fournier D 1981 *Appl. Opt.* **20** 1333–44
- [5] Salazar A, Sanchez-Lavega A and Fernandez J 1993 *J. Appl. Phys.* **74** 1539–47
- [6] Xiao L et al 2008 *Nano Lett.* **8** 4539–45
- [7] Aliev A E, Lima M D, Fang S and Baughman R H 2010 *Nano Lett.* **10** 2374–80
- [8] Gottlieb M, Ireland C L M and Ley J M 1983 *Electro-Optic and Acousto-Optic Scanning and Deflection* (New York: Dekker)
- [9] Miller J L and Friedman E 2004 *Photonics Rules of Thumb: Optics, Electro-Optics, Fiber Optics, and Lasers* (New York: McGraw-Hill)
- [10] Zhang M, Fang S L, Zakhidov A A, Lee S B, Aliev A E, Williams C D, Atkinson K R and Baughman R H 2005 *Science* **309** 1215–9
- [11] Lide D R (ed) 2001–2002 *CRC Handbook of Chemistry and Physics* 82nd edn (New York: CRC Press)
- [12] Fan Y, Singer S B, Bergstrom R and Regan B C 2009 *Phys. Rev. Lett.* **102** 187402
- [13] Aliev A E, Guthy C, Zhang M, Fang S L, Zakhidov A A, Fischer J E and Baughman R H 2007 *Carbon* **45** 2880–8
- [14] Aliev A E, Lima M D, Silverman E M and Baughman R H 2010 *Nanotechnology* **21** 035709
- [15] Liu P, Liu L, Wei Y, Liu K, Chen Zh, Jiang K, Li Q and Fan Sh 2009 *Adv. Mater.* **21** 3563–6